

The long-term stability of extrasolar system HD 37124. Numerical study of resonance effects.

Krzysztof Goździewski¹*, Sławomir Breiter²†, Wojciech Borczyk²‡

7 November 2018

ABSTRACT

We describe numerical tools for the stability analysis of extrasolar planetary systems. In particular, we consider the relative Poincaré variables and symplectic integration of the equations of motion. We apply the tangent map to derive a numerically efficient algorithm of the fast indicator MEGNO (a measure of the maximal Lyapunov exponent) that helps to distinguish chaotic and regular configurations. The results concerning the three-planet extrasolar system HD 37124 are presented and discussed. The best fit solutions found in earlier works are studied more closely. The system involves Jovian planets with similar masses. The orbits have moderate eccentricities, nevertheless the best fit solutions are found in dynamically active region of the phase space. The long term stability of the system is determined by a net of low-order two-body and three-body mean motion resonances. In particular, the three-body resonances may induce strong chaos that leads to self-destruction of the system after Myrs of apparently stable and bounded evolution. In such a case, numerically efficient dynamical maps are useful to resolve the fine structure of the phase space and to identify the sources of unstable behavior.

Key words: extrasolar planets—Doppler technique—stars:individual HD 37124—N-body problem—numerical methods

1 INTRODUCTION

Understanding the extrasolar planetary systems has became a major challenge for contemporary astronomy. One of the most difficult problems in this field concerns the orbital stability of such systems. Usually, the investigations of long-term evolution are the domain of direct, numerical integrations. The stability of extrasolar systems is often understood in terms of the Lagrange definition implying that orbits remain well bounded over an arbitrarily long time. Other definitions may be formulated as well, like the astronomical stability (Lissauer 1999) requiring that the system persists over a very long, Gyr time-scale, or Hill stability (Szebehely 1984) that requires the constant ordering of the planets. In our studies, we prefer a more formal and stringent approach related to the fundamental Kolmogorov-Arnold-Theorem (KAM), see Arnold (1978). Planetary systems, involving a dominant mass of the parent star and significantly smaller planetary masses, are well modeled by close-to-integrable, Hamiltonian dynamical systems. It is well known, that their evolution may be quasi-periodic (with a discrete number of fundamental frequencies, forever stable), periodic (or resonant;

stable or unstable) or chaotic (with a continuous spectrum of frequencies, and unstable). In the last case, initially close phase trajectories diverge exponentially, i.e., their Maximum Lyapunov Characteristic Exponent (MLCE, denoted also with σ) is positive. In general, the distinction between regular and chaotic trajectories is a very difficult task that may be resolved only with numerical methods relying on efficient and accurate integrators of the equations of motion.

The main motivation of this paper is to describe numerical tools that are useful for studies of the dynamical stability and to apply them to the HD 37124 system (Vogt et al. 2005). We recall the fundamentals of relative canonical Poincaré variables as – in our opinion – one of the best frameworks for symplectic integrators. These canonical variables are well suited for the construction of a Laskar & Robutel (2001) composition method that improves a classical Wisdom-Holman (W-H) algorithm (Wisdom & Holman 1991). We supplement the integrator with a propagator of the associated symplectic tangent map that approximates the solution of variational equations (Mikkola & Innanen 1999). Finally, we compare two fast indicators that reveal the character of phase trajectories. The first one is a relatively simple method for resolving fundamental frequencies and spectral properties of a close-to-integrable Hamiltonian system – a so called Spectral Number (SN), invented by Michtchenko & Ferraz-Mello (2001). The second indicator belongs to the realm of the Lyapunov exponent based algorithms; we chose the numerical tool developed by Cincotta & Simó (2000); Cincotta et al. (2003) under the name of MEGNO. In this work,

* Toruń Centre for Astronomy, N. Copernicus University, Poland, k.gozdziewski@astro.uni.torun.pl

† Astronomical Observatory of A. Mickiewicz University, Słoneczna 36, PL 60-286 Poznań, Poland, breiter@amu.edu.pl

‡ Astronomical Observatory of A. Mickiewicz University, Słoneczna 36, PL 60-286 Poznań, Poland, bori@moon.astro.amu.edu.pl

we refine the algorithm of MEGNO that makes explicit use of the symplectic tangent map (Goździewski 2003).

As a non-trivial application of the presented numerical tools, we consider the 3-planet system hosted by the HD 37124 star (Vogt et al. 2005). It has been discovered by the radial velocity (RV) technique. The recent model of the RV observations of HD 37124 predicts three equal Jovian type planets with masses $\sim 0.6 m_J$ in orbits with moderate eccentricities. In such a case, the application of symplectic integrators without regularization is particularly advantageous thanks to the numerical efficiency (long time-steps) and accuracy (the total energy does not have a secular error and the angular momentum integral is conserved). The number of multi-planet systems resembling the architecture of the Solar system increases¹. Hence, our approach may be useful in other cases.

2 NUMERICAL TOOLS

According to the classical results of celestial mechanics, the N -body problem has only 10 integrals of motion for all $N > 2$; they consist of 6 integrals of barycenter, 3 integrals of angular momentum and the energy integral. The integrals of barycenter play a very particular role in the studies of an N -body system dynamics. First, they define the origin of an inertial reference frame in terms of the mutual distances and velocities of the bodies considered, thus dismissing the need of some extrinsic absolute frame. But what is more important, being linear forms of coordinates and momenta they allow a unique reduction of the system, lowering the number of degrees of freedom by three, with no loss of information. This is why we can solve the relative two-body problem and then recover the motion of both masses with respect to their center of mass. And this is why we can approximately solve the heliocentric motion of planets, recovering the barycentric evolution *a posteriori*.

Within the framework of Hamiltonian mechanics, the reduction is usually achieved by means of a transformation to one of the two common variable types: relative Jacobi variables, or "heliocentric" Poincaré variables (Whittaker 1952, Ch. XIII). We focus on the latter set, because it offers the best choice in many aspects. We introduce the basic ideas related to the Poincaré variables and we derive them as a Mathieu transformation; this way is simpler and more intuitive than the procedure based upon a generating function that was presented by Whittaker (1952, p. 343) or Duncan et al. (1998). Then we discuss the setup of the Hamiltonian within the framework of Wisdom-Holman type integrators.

2.1 Poincaré variables basics

Let us consider a system consisting of $N+1$ material points with masses m_0, \dots, m_N . We define a barycentric position vector $\mathbf{p} \in \mathbb{R}^{3N}$ and its canonical conjugate momentum $\mathbf{P} \in \mathbb{R}^{3N}$ as

$$\mathbf{p} = \begin{bmatrix} \mathbf{p}_0 \\ \mathbf{p}_1 \\ \vdots \\ \mathbf{p}_N \end{bmatrix}, \quad \mathbf{P} = \begin{bmatrix} \mathbf{P}_0 \\ \mathbf{P}_1 \\ \vdots \\ \mathbf{P}_N \end{bmatrix}. \quad (1)$$

Then, the barycentric equations of motion can be derived from the Hamiltonian function (Laskar 1990)

¹ For a recent statistics of the discoveries, see Jean Schneider's Extrasolar Planets Encyclopedia, <http://exoplanets.eu>.

$$\mathcal{H}(\mathbf{p}, \mathbf{P}) = \sum_{i=0}^N \frac{\mathbf{P}_i^2}{2m_i} - \sum_{i=0}^N \sum_{j=i+1}^N \frac{k^2 m_i m_j}{\Delta_{ij}}, \quad (2)$$

where the mutual distance Δ_{ij} is

$$\Delta_{ij} = \|\mathbf{p}_j - \mathbf{p}_i\|, \quad (3)$$

and k stands for the Gaussian gravity constant.

The Hamiltonian (2) admits six integrals of barycenter

$$\sum_{i=0}^N m_i \mathbf{p}_i = \mathbf{0}, \quad \sum_{i=0}^N \mathbf{P}_i = \mathbf{0}, \quad (4)$$

as well as the energy integral $\mathcal{H} = \text{const}$, and three angular momentum integrals

$$\mathbf{G} = \sum_{i=0}^N \mathbf{p}_i \times \mathbf{P}_i = \mathbf{const}. \quad (5)$$

The integrals are usually exploited as the accuracy control tool when the differential equations of motion

$$\dot{\mathbf{p}} = \frac{\partial \mathcal{H}}{\partial \mathbf{P}}, \quad \dot{\mathbf{P}} = -\frac{\partial \mathcal{H}}{\partial \mathbf{p}}, \quad (6)$$

are solved numerically.

Instead of solving the $6N+6$ order system (6), it is often desirable to study the relative motion of N bodies with respect to the material point m_0 . But if the integration method to be applied is symplectic, it is necessary to use the Hamiltonian equations of motion, hence the necessity of defining a canonical transformation $(\mathbf{p}, \mathbf{P}, \mathcal{H}) \leftrightarrows (\mathbf{r}, \mathbf{R}, \mathcal{K})$ with new, relative coordinates \mathbf{r} and momenta \mathbf{R} .

A naive, straightforward approach would consist in postulating $\mathbf{r}_i = \mathbf{p}_i - \mathbf{p}_0$ for all i . This leads to $\mathbf{r}_0 = \mathbf{0}$ and the Jacobian matrix of the transformation becomes singular; such a transformation cannot be canonical regardless of the choice of the momenta. However, the difficulty can be easily circumvented if we change the definition of \mathbf{r}_0 . Poincaré (1896) proposed

$$\begin{aligned} \mathbf{r}_i &= \mathbf{p}_i - \mathbf{p}_0, & \text{for } i = 1, \dots, N, \\ \mathbf{r}_0 &= \mathbf{p}_0, \end{aligned} \quad (7)$$

whereas Duncan et al. (1998) chose \mathbf{r}_0 as the position of the barycenter in some arbitrary inertial frame. For the barycentric system, the latter choice amounts to a "differentiable zero" $\mathbf{r}_0 = (\sum_{i=0}^N m_i)^{-1} \sum_{i=0}^N m_i \mathbf{p}_i = \mathbf{0}$. It turns out, that both starting points lead to the same result, so we continue our presentation assuming the Poincaré choice (7).

Retaining \mathbf{r}_0 as the position of the reference body m_0 with respect to the barycenter, we can perform a canonical extension of the time-independent point transformation (7), requesting the Mathieu transformation condition (Whittaker 1952, p. 301)

$$\mathbf{P} \cdot d\mathbf{p} = \mathbf{R} \cdot d\mathbf{r}, \quad (8)$$

or, explicitly,

$$\sum_{i=0}^N \mathbf{P}_i \cdot d\mathbf{p}_i = \mathbf{R}_0 \cdot d\mathbf{p}_0 + \sum_{i=1}^N \mathbf{R}_i \cdot (d\mathbf{p}_i - d\mathbf{p}_0). \quad (9)$$

Equating the coefficient of each differential $d\mathbf{p}_i$ to zero, we find the new momenta

$$\begin{aligned} \mathbf{R}_i &= \mathbf{P}_i, & \text{for } i = 1, \dots, N, \\ \mathbf{R}_0 &= \sum_{i=0}^N \mathbf{P}_i = \mathbf{0}. \end{aligned} \quad (10)$$

The fact, that $\mathbf{R}_0 = \mathbf{0}$ is a direct consequence of the integrals of barycenter (4).

Equations (7) and (10), that are due to Poincaré (1896), define the canonical relative variables. The coordinates \mathbf{r} consist of the positions with respect to the reference body m_0 , save for the \mathbf{r}_0 that is measured with respect to the barycenter. The momenta \mathbf{R} are measured with respect to the barycenter, save for \mathbf{R}_0 that can be understood as measured with respect to m_0 and hence it is zero (although with nonvanishing partials with respect to \mathbf{P}_i).

The most important feature is that the new Hamiltonian \mathcal{K} , obtained by the simple substitution of the transformation equations into \mathcal{H} , does not depend neither on the coordinates, nor on the momenta of m_0 . Indeed, one obtains (Poincaré 1896; Whittaker 1952; Hagihara 1970; Deprit 1983; Laskar 1990, 1991)

$$\begin{aligned} \mathcal{K} = & \frac{1}{2} \sum_{i=1}^N \left(\frac{1}{m_0} + \frac{1}{m_i} \right) \mathbf{R}_i^2 + \frac{1}{m_0} \sum_{i=1}^N \sum_{j=i+1}^N \mathbf{R}_i \cdot \mathbf{R}_j - \\ & - \sum_{i=1}^N \frac{k^2 m_0 m_i}{r_i} - \sum_{i=1}^N \sum_{j=i+1}^N \frac{k^2 m_i m_j}{\Delta_{ij}}, \end{aligned} \quad (11)$$

where $\Delta_{ij} = \|\mathbf{p}_j - \mathbf{p}_i\| = \|\mathbf{r}_j - \mathbf{r}_i\|$, or, equivalently (Duncan et al. 1998; Chambers 1999)

$$\begin{aligned} \mathcal{K} = & \frac{1}{2} \sum_{i=1}^N \frac{1}{m_i} \mathbf{R}_i^2 + \frac{1}{2m_0} \left(\sum_{i=1}^N \mathbf{R}_i \right)^2 - \\ & - \sum_{i=1}^N \frac{k^2 m_0 m_i}{r_i} - \sum_{i=1}^N \sum_{j=i+1}^N \frac{k^2 m_i m_j}{\Delta_{ij}}. \end{aligned} \quad (12)$$

An important fact to be remembered is that the Hamiltonian \mathcal{K} has the form (11) or (12) only if the substitution of the barycenter integrals (4) has been performed. Thus it cannot serve to obtain the equations for $\dot{\mathbf{r}}_0$ or $\dot{\mathbf{R}}_0$. However, once we know all the remaining \mathbf{r}_i and \mathbf{R}_i , the \mathbf{r}_0 values can be easily computed from Equations (4) and (7), whereas $\mathbf{R}_0 = \mathbf{0}$ by the definition. For all the remaining bodies

$$\dot{\mathbf{r}}_i = \frac{\partial \mathcal{K}}{\partial \mathbf{R}_i}, \quad \dot{\mathbf{R}}_i = -\frac{\partial \mathcal{K}}{\partial \mathbf{r}_i}, \quad (13)$$

and we will assume that $i = 1, \dots, N$ throughout the rest of this paper.

A remarkable property of the Poincaré variables is

$$\mathbf{G} = \sum_{i=0}^N \mathbf{p}_i \times \mathbf{P}_i = \sum_{i=1}^N \mathbf{r}_i \times \mathbf{R}_i, \quad (14)$$

which means, that the total angular momentum of the reduced system of N bodies evaluated by means of the Poincaré variables is the same as the angular momentum of $N+1$ bodies evaluated in the barycentric frame.

If the reference body mass $m_0 \gg m_i$, the Hamiltonian \mathcal{K} can be easily partitioned into the unperturbed, Keplerian part and a small perturbation proportional to the greatest of m_i . From the point of view of analytical theories using these variables (Yuasa & Hori 1979; Hori 1985), it is preferable to split \mathcal{K} into the sum

$$\mathcal{K} = \mathcal{K}_0^{(a)} + \mathcal{K}_1^{(a)}, \quad (15)$$

where (Laskar 1990, 1991)

$$\mathcal{K}_0^{(a)} = \frac{1}{2} \sum_{i=1}^N \frac{m_0 + m_i}{m_0 m_i} \mathbf{R}_i^2 - \sum_{i=1}^N \frac{k^2 m_0 m_i}{r_i}, \quad (16)$$

$$\mathcal{K}_1^{(a)} = \frac{1}{m_0} \sum_{i=1}^N \sum_{j=i+1}^N \mathbf{R}_i \cdot \mathbf{R}_j - \sum_{i=1}^N \sum_{j=i+1}^N \frac{k^2 m_i m_j}{\Delta_{ij}}. \quad (17)$$

The principal part $\mathcal{K}_0^{(a)}$ defines N relative two-body problems. The perturbation $\mathcal{K}_1^{(a)}$ involves not only the mutual interactions between the minor bodies m_i , but also the momenta related terms that replace the usual "indirect part" of the perturbing function present in noncanonical relative $(N+1)$ -body problem (Poincaré 1905). It is due to this term, that the Poincaré variables were considered somehow handicapped; the objection that velocities are no longer tangent to the momenta became almost a proverb, although many non-inertial reference frames have the same property, the restricted three-body problem being the best example. This objection has fortunately ceased to be taken seriously; for example, Ferraz-Mello et al. (2004) successfully use orbital elements evaluated from the Poincaré momenta \mathbf{R} . In this paper we will use alternatively two types of orbital elements. The *osculating elements* are computed by the usual two body formulae from astrocentric positions \mathbf{r}_i and velocities $\dot{\mathbf{r}}_i$; we use them in all plot labels and orbital data tables. But in the calculation of spectral numbers or in the definitions of resonance arguments, we use orbital elements computed from \mathbf{r}_i and $m_0 m_i / (m_0 + m_i) \mathbf{R}_i$, calling them *contact elements* after Brumberg (1991). [In fact, the transformation between astrocentric positions – barycentric momenta and the contact elements can be still done with the usual two-body formulae (Morbidelli 2002)]. The former are commonly used in literature, whereas the latter offer a better behavior from the dynamical point of view. The superiority of contact elements results from the fact, that the reference frame of Cartesian momenta is inertial, hence the influence of noninertial forces is reduced to purely kinematical contribution. The inferred Keplerian angles $(\omega, \Omega, \mathcal{M})$ and the conjugate momenta can be interpreted as canonical Delaunay's elements (Morbidelli 2002), so the derivation and interpretation of the fundamental frequencies is straightforward.

2.2 Symplectic integration: two is a company

With the advent of symplectic integrators based on the Wisdom-Holman approach (Wisdom & Holman 1991), the Poincaré variables became an attractive framework for the numerical studies of planetary systems (Duncan et al. 1998; Chambers 1999). First of all, similarly to the Jacobian coordinates, they reduce the number of equations of motion by 6 with respect to the barycentric problem. Thanks to the possibility of splitting \mathcal{K} into the main part and a perturbation, they also allow the construction of a symplectic integrator with the local truncation error proportional to the product of m_i/m_0 , hence a larger integration step h can be applied.

Given a Hamiltonian $\mathcal{M} = \mathcal{M}_0 + \varepsilon \mathcal{M}_1$ with a small parameter ε , the W-H integrator is based on the alternating application of maps $\Phi_{0,\tau}(\mathbf{r}, \mathbf{R})$ and $\Phi_{1,\tau}(\mathbf{r}, \mathbf{R})$ that represent the solutions of equations of motion derived from \mathcal{M}_0 and $\varepsilon \mathcal{M}_1$ alone, on the interval from t_0 to $t_0 + \tau$. Moreover, each of the Hamiltonian parts should admit (a possibly simple) analytical solution of the equations of motion.

In the numerical applications, Hamiltonian \mathcal{K} is typically split differently than in Equation (15), namely (Duncan et al. 1998; Chambers 1999)

$$\mathcal{K} = \mathcal{K}_0 + \mathcal{K}_1, \quad (18)$$

where

$$\mathcal{K}_0 = \frac{1}{2} \sum_{i=1}^N \frac{1}{m_i} \mathbf{R}_i^2 - \sum_{i=1}^N \frac{k^2 m_0 m_i}{r_i}, \quad (19)$$

$$\mathcal{K}_1 = \frac{1}{2m_0} \left(\sum_{i=1}^N \mathbf{R}_i \right)^2 - \sum_{i=1}^N \sum_{j=i+1}^N \frac{k^2 m_i m_j}{\Delta_{ij}}. \quad (20)$$

The unperturbed part \mathcal{K}_0 has now a different meaning: it still leads to N relative two-body problems

$$\dot{\mathbf{r}}_i = \frac{\partial \mathcal{K}_0}{\partial \mathbf{R}_i} = \frac{\mathbf{R}_i}{m_i}, \quad (21)$$

$$\dot{\mathbf{R}}_i = -\frac{\partial \mathcal{K}_0}{\partial \mathbf{r}_i} = -\frac{k^2 m_0 m_i}{r_i^3} \mathbf{r}_i, \quad (22)$$

but this time they are the *restricted* two-body problems with negligible masses m_i or a fixed center of gravity:

$$\ddot{\mathbf{r}}_i = -\frac{k^2 m_0}{r_i^3} \mathbf{r}_i. \quad (23)$$

The perturbation part \mathcal{K}_1 remains proportional to m_i/m_0 and it is still a function of both coordinates \mathbf{r} and momenta \mathbf{R} . Duncan et al. (1998) and then Chambers (1999) considered it an obstacle, so they further split \mathcal{K}_1 into

$$\mathcal{K}_1 = \mathcal{K}_{11}(\mathbf{R}) + \mathcal{K}_{12}(\mathbf{r}), \quad (24)$$

obtaining elementary "kick" maps $\Phi_{11,\tau}$

$$\mathbf{r}'_i = \mathbf{r}_i + \frac{\tau}{m_0} \sum_{j=1}^N \mathbf{R}_j, \quad (25)$$

$$\mathbf{R}'_i = \mathbf{R}_i. \quad (26)$$

and $\Phi_{12,\tau}$

$$\mathbf{r}'_i = \mathbf{r}_i, \quad (27)$$

$$\mathbf{R}'_i = \mathbf{R}_i - \tau \sum_{j=1, j \neq i}^N \frac{k^2 m_i m_j}{\Delta_{ij}^3} (\mathbf{r}_i - \mathbf{r}_j). \quad (28)$$

In the formulas of both maps we add a prime to the symbols standing for the values of coordinates and momenta at $t_0 + \tau$, whereas unprimed symbols refer to the values at t_0 .

As the effect of the partition (24), the classical "leapfrog"

$$\Phi_\tau \approx \Phi_{1,\tau/2} \circ \Phi_{0,\tau} \circ \Phi_{1,\tau/2}, \quad (29)$$

was replaced by

$$\Phi_\tau \approx \Phi_{11,\tau/2} \circ \Phi_{12,\tau/2} \circ \Phi_{0,\tau} \circ \Phi_{12,\tau/2} \circ \Phi_{11,\tau/2}. \quad (30)$$

According to Duncan et al. (1998), the ordering of Φ_{11} and $\Phi_{12,\tau}$ is insignificant, and, indeed, Chambers (1999) interchanged them, using

$$\Phi_\tau \approx \Phi_{12,\tau/2} \circ \Phi_{11,\tau/2} \circ \Phi_{0,\tau} \circ \Phi_{11,\tau/2} \circ \Phi_{12,\tau/2}. \quad (31)$$

The interchange of the maps is justified by the fact that \mathcal{K}_{11} and \mathcal{K}_{12} commute, i.e. the Poisson bracket $\{\mathcal{K}_{11}; \mathcal{K}_{12}\} = 0$. In these circumstances

$$\Phi_{1,\tau} = \Phi_{12,\tau} \circ \Phi_{11,\tau} = \Phi_{11,\tau} \circ \Phi_{12,\tau}, \quad (32)$$

and we can concatenate both maps obtaining $\Phi_{1,\tau}$ in a compact form.

$$\mathbf{r}'_i = \mathbf{r}_i + \frac{\tau}{m_0} \sum_{j=1}^N \mathbf{R}_j \quad (33)$$

$$\mathbf{R}'_i = \mathbf{R}_i - k^2 m_i \tau \sum_{j=1, j \neq i}^N \frac{m_j (\mathbf{r}_i - \mathbf{r}_j)}{\Delta_{ij}^3}, \quad (34)$$

where \mathbf{r}_i stands for $\mathbf{r}_i(t_0)$, \mathbf{r}'_i stands for $\mathbf{r}_i(t_0 + \tau)$, and similarly for \mathbf{R}_i , \mathbf{R}'_i .

Separating \mathcal{K} according to Equations (18), (19), and (20) offers a possibility of using only two maps for a W-H integrator. Although our partitioning seems to be more compact and clear than the "heliocentric-democratic" scheme, we note that both mappings are practically equivalent as far as the CPU cost is concerned. Yet the rule "two is a company, three is a crowd" holds true in the realm of symplectic integrators for perturbed systems: according to the theorem of Suzuki (1991) any symplectic composition method of an order higher than 2 must necessarily involve stages with negative sub-steps that amplify accumulation of roundoff errors. This holds true for a composition of maps derived from splitting the Hamiltonian into any number of terms. However, Laskar & Robutel (2001) found a family of methods designed for two-terms perturbed systems with $\mathcal{K} = \mathcal{A} + \varepsilon \mathcal{B}$ where the negative sub-steps are avoided. Their integrators do not contradict the results of Suzuki: formally they remain second order methods, but in contrast to other W-H methods with local truncation errors $O(\varepsilon \tau^2)$, their errors have a form $O(\varepsilon^2 \tau^2 + \varepsilon \tau^n)$. So, for sufficiently small perturbation ε , the Laskar-Robutel methods may behave like higher order integrators in certain domain of stepsize τ although no negative substeps were introduced.

2.3 Tangent maps

Whenever a differential correction of initial conditions or the computation of sensitivity indicators is required, the use of tangent maps becomes indispensable. Keplerian map Φ_0 and its associate tangent map can be computed according to a comprehensive recipe by Mikkola & Innanen (1999). The propagation of a tangent vector

$$\xi = \begin{pmatrix} \delta \mathbf{r} \\ \delta \mathbf{R} \end{pmatrix}, \quad (35)$$

under the action of the "kick" map Φ_1 amounts to multiplying it by the Jacobian matrix $D\Phi_1$. Resulting expressions are simple:

$$\delta \mathbf{r}' = \delta \mathbf{r} + \frac{\tau}{m_0} \sum_{j=1}^N \delta \mathbf{R}_j, \quad (36)$$

$$\delta \mathbf{R}'_i = \delta \mathbf{R}_i + \tau k^2 m_i \sum_{j=1, j \neq i}^N \frac{m_j}{\Delta_{ij}^3} \left[\delta_{ij} + \frac{3 \delta \Delta_{ij}}{\Delta_{ij}} (\mathbf{r}_i - \mathbf{r}_j) \right], \quad (37)$$

where

$$\delta \Delta_{ij} = \frac{(\mathbf{r}_j - \mathbf{r}_i) \cdot \delta_{ij}}{\Delta_{ij}}, \quad \delta_{ij} = \delta \mathbf{r}_j - \delta \mathbf{r}_i. \quad (38)$$

2.4 Angular momentum integral

It can be easily demonstrated, that any composition of maps Φ_0 and Φ_1 conserves the angular momentum integral (14). This property is guaranteed by the conservation of \mathbf{G} by each map separately. Recalling that Φ_0 and Φ_1 define *exact* solutions of motion generated by \mathcal{K}_0 and \mathcal{K}_1 respectively, we can simply check that

$$\{\mathbf{G}; \mathcal{K}_0\} = \{\mathbf{G}; \mathcal{K}_1\} = \mathbf{0}. \quad (39)$$

The proof of Eq. (39) is straightforward. Starting from the definition of \mathbf{G} , we use the linearity of Poisson brackets and the Leibnitz identity to write

$$\{\mathbf{G}; \mathcal{K}_0\} = \sum_{i=1}^N \mathbf{r}_i \times \{\mathbf{R}_i; \mathcal{K}_0\} - \mathbf{R}_i \times \{\mathbf{r}_i; \mathcal{K}_0\} =$$

$$= - \sum_{i=1}^N \mathbf{r}_i \times \frac{\partial \mathcal{K}_0}{\partial \mathbf{r}_i} + \mathbf{R}_i \times \frac{\partial \mathcal{K}_0}{\partial \mathbf{R}_i}. \quad (40)$$

Then we substitute the right-hand sides of Equations (21) and (22), concluding that all vector products vanish and indeed $\{\mathbf{G}; \mathcal{K}_0\} = \mathbf{0}$. A similar procedure demonstrates $\{\mathbf{G}; \mathcal{K}_1\} = \mathbf{0}$.

Of course, from practical point of view the conservation of \mathbf{G} is only up to computer roundoff errors.

2.5 Chaoticity indicators

To detect unstable motions in the phase space, many numerical tools are available. Concerning the dynamics of close-to-integrable Hamiltonian systems, they can be roughly divided in two classes: spectral algorithms that resolve the fundamental frequencies and/or their diffusion rates (Laskar 1993; Šidlichovský & Nesvorný 1997; Michtchenko & Ferraz-Mello 2001), and methods based on the divergence rate of initially close phase trajectories, expressed in terms of the Lyapunov exponents (Benettin et al. 1980; Froeschlé 1984).

In this work, among the the spectral tools, we choose the method invented by Michtchenko & Ferraz-Mello (2001); its idea is genuinely simple — to detect chaotic behavior one counts the number of frequencies in the FFT-spectrum of an appropriately chosen dynamical signal. We deal with conservative Hamiltonian systems; so in a regular case, the spectrum of fundamental frequencies is discrete and we obtain only a few dominant peaks in the FFT spectrum. Chaotic signals do not have well defined frequencies, and their FFT spectrum is very complex. The number of peaks in the spectrum above some noise level p (typically, p is set to a few percent of the dominant amplitude) tell us on the character (regular, chaotic) of the of the system.

The method by Michtchenko & Ferraz-Mello (2001) does not have as strong theoretical foundations as the Frequency Map Analysis (FMA) by Laskar (1993) or the Fourier Modified Transform (FMT) by Šidlichovský & Nesvorný (1997) which are considered as rigorous and efficient tools. We did some comparative tests of the later algorithm with MEGNO already (Goździewski & Konacki 2004). Here, we choose the method of Michtchenko & Ferraz-Mello (2001) for its appealing simplicity and because we used it in the former papers devoted to the analysis of the RV data. In that way, we can compare the results directly. In our code, the spectral signals analyzed with the FFT are related to canonical Poincaré elements, so the fundamental frequencies are well defined. Moreover, we resolve the chaotic and regular signals by comparing the number of significant peaks in the FFT spectrum, thus a very precise determination of the fundamental frequencies is not critical. Actually, in this work we also show that the algorithm has same drawbacks and should be applied with care.

The basic tool to discover exponentially unstable bounded orbits, i.e. chaotic orbits, is the Maximum Lyapunov Characteristic Exponent (MLCE) σ . Numerical symplectic integration methods are fixed step algorithms, so we can restrict our discussion to the iterations of a discrete map $\zeta_n = \Phi^n \zeta_0$, that generates a sequence of state vectors ζ_n consisting of coordinates and their conjugate momenta. The direct computation of the MLCE is based on the analysis of the tangent vectors δ_n that evolve under the action of a linear tangent map $\delta_n = (D\Phi)^n \delta_0$. Asymptotically, the MLCE value is given by

$$\sigma = \lim_{n \rightarrow \infty} \frac{1}{n} \sum_{k=1}^n \ln \left(\frac{\delta_k}{\delta_{k-1}} \right). \quad (41)$$

If σ converges to some positive value, we conclude that the nominal orbit ζ_n and some initially close orbit diverge exponentially at the rate $\exp(\sigma t)$. Two practical difficulties arise when the direct definition (41) is used: the convergence of σ is often very slow, and it is difficult to tell how small should be the final value of σ to consider it $\sigma = 0$.

A large variety of methods has been proposed to overcome the problem of slowly convergent MLCE estimates. The authors prefer the so called MEGNO (Mean Exponential Growth factor of Nearby Orbits) indicator proposed by Cincotta & Simó (2000) — that choice is justified by the successful application of this method in our previous works (e.g., Breiter et al. 2005; Goździewski et al. 2006, and the references therein). The definition of MEGNO for a discrete map is (Cincotta et al. 2003)

$$Y(n) = \frac{1}{n} \sum_{k=1}^n y(k), \quad (42)$$

where

$$y(n) = \frac{2}{n} \sum_{k=1}^n k \ln \left(\frac{\delta_k}{\delta_{k-1}} \right). \quad (43)$$

If the iterates of the discrete map refer to the moments of time separated by the stepsize h , the discrete map MEGNO function $Y(n)$ asymptotically tends to

$$Y_n = ah + b,$$

with $a = 0, b = 2$ for a quasi-periodic orbit, $a = b = 0$ for a stable, isochronous periodic orbit, and $a = \frac{1}{2}\sigma, b = 0$ for a chaotic orbit. Thus we can indirectly estimate the MLCE on a finite time interval, but the weight function k in the sum (43) reduces the contribution of the initial part of the tangent vector evolution, when the exponential divergence is to small to be observed behind other linear and non-linear effects (Morbidelli 2002). Thus, fitting the straight line to the final part of $Y(n)$, we obtain good estimates of σ from a relatively shorter piece of trajectory than in the direct MLCE evaluation.

In practical application, one can use a more convenient form of Eqs. (42) and (43) proposed by Breiter et al. (2005)

$$Y(n) = \frac{(n-1)Y(n-1) + y(n)}{n}, \quad (44)$$

$$y(n) = \frac{n-1}{n} y(n-1) + 2 \ln \left(\frac{\delta_n}{\delta_{n-1}} \right), \quad (45)$$

with the initial setup $y(0) = Y(0) = 0$. The fact that only the ratio δ_n/δ_{n-1} is significant, as well as the linearity of tangent map, allows to avoid the overflow of δ_n thanks to occasional normalization of the tangent vector length to $\delta_n = 1$ performed after the ratio of δ_n/δ_{n-1} has been evaluated.

3 STABILITY OF THE HD 37124 PLANETARY SYSTEM

As a non-trivial application of the presented algorithms and the illustration of difficulties arising in the dynamical analysis of the long-term stability of multiplanet configurations, we choose the HD 37124 extrasolar system. The discovery of two Jovian planets has been announced by Butler et al. (2001) and confirmed by Vogt et al. (2005). At first, the system seemed to be well modeled by a 2-planet configuration (Butler et al. 2001). However, new observations lead to two-planet fits with $e_c \sim 0.7$ and a catastrophically unstable configuration. Moreover, with the updated RV observations, Vogt et al. (2005) found much better model of 3 planets

Table 1. The best-fit astro-centric, osculating Keplerian elements of a stable HD 37124 planetary configuration at the epoch of the first observation $t_0 = \text{JD}2,451,0420.047$. Mass of the parent star is $0.78 m_\odot$. The fit has been refined with GAMP over $\sim 5 \cdot 10^4 P_d$. See (Vogt et al. 2005; Goździewski et al. 2006) and Fig. 2 for more details.

Parameter	planet b	planet c	planet d
$m \sin i$ [mj]	0.62447	0.56760	0.71194
a [AU]	0.51866	1.61117	3.14451
e	0.07932	0.15267	0.29775
ω [deg]	138.405	268.863	269.494
$\mathcal{M}(t_0)$ [deg]	259.011	109.545	124.113
$(\chi^2_\nu)^{1/2}$		0.938	
V_0 [m s ⁻¹]		7.629	
rms [m s ⁻¹]		3.39	

with similar masses of $\sim 0.6 m_j$ in low-eccentric orbits. The best fits have the rms ~ 4 m/s, in agreement with the internal accuracy of the data. However, the best-fit orbital solution, both in the the kinematic Keplerian model, and in more realistic N -body simulation (see Table 1), lies close to the collision line of planets c and d. Note, that we define the collision line in terms of semi-axes and eccentricities as $a_c(1+e_c) = a_d(1-e_d)$. This line marks the zone in which the mutual interactions of massive companions can quickly destabilize the system.

How to interpret the RV measurements remains an open question. The dynamical long-term stability of the planetary system is the most natural requirement of a configuration consistent with observations. Yet the three-planet model is parameterized by at least 16 parameters, even assuming that the system is coplanar. For that reason the search for the best fits fulfilling the constraints of stability is a difficult task. It can be resolved in different ways. For example, we may try to find dynamically stable solutions in the vicinity of the formal best fit configurations (the latter are often unstable). However, examining the stability of configurations in that neighborhood, we have no reasons to expect that the stable fits are optimal in the statistical sense. Another approach relies on the elimination of unstable fits *during* the fitting process, through *penalizing* unstable solutions with a large value of $(\chi^2_\nu)^{1/2}$. This method, described in Goździewski et al. (2006), is dubbed GAMP (Genetic Algorithm with MEGNO Penalty). It was shown, that such an approach is particularly useful in modeling resonant or close-to-resonant planetary configurations. Unfortunately, the algorithm cannot give definite answer when we want to resolve the $(\chi^2_\nu)^{1/2}$ shape of strictly stable solutions in detail. The penalty term in the $(\chi^2_\nu)^{1/2}$ function relies on a signature of the system stability, expressed through the fast indicator. Due to significant CPU overhead, the fast indicator in the minimizing code can be only calculated over relatively short time, typically 10^3 orbital periods of the outermost planet. Moreover, the code can converge to unstable best fits that appear stable on that short time scale. Hence, at the end of the search, we have to examine the stability of the individual best fits in the obtained ensemble of solutions, over the time-scale of relevant mean motion and secular resonances.

3.1 Long-term stability of the best-fit configurations

The GAMP analysis of the RV data of HD 37124 published by Vogt et al. (2005) was presented in Goździewski et al. (2006). About 100 of best fit solutions were found yielding $(\chi^2_\nu)^{1/2} < 1.1$, the rms ~ 4 m/s, and *stable* in the sense that their MEGNO signa-

tures are close to 2 up to $\sim 1000 - 2000$ orbital periods of the outermost planet. Due to heavy CPU requirements, the time-span to resolve MEGNO in the GAMP code cannot be set very long. The short integration time $\sim 10^3 P_d$ allows only to eliminate strongly chaotic configurations, typically leading to collisions between planets and/or with the parent star. The best fit solutions were found in a dynamically active region of the phase space, spanned by a number of low-order mean motion resonances (MMRs) between the two outermost Jovian companions, like 5c:2d, 8c:3d, or 11c:4d (see Fig. 2 and dynamical maps presented in Figs. 3,4,5,6). In particular, close to the collision lines, the low-order MMRs overlap, giving rise to the global instability zone.

Yet we should be aware that two-body MMRs with characteristic time scale $\sim 10^4 - 10^5$ orbital periods of the outermost planet are not the only source of instability in the multi-planet system. Already when we deal with three-planet configurations, the strong instabilities may be generated by three-body MMRs or by long-term secular resonances (Nesvorný & Morbidelli 1998, 1999; Murray et al. 1998; Guzzo 2006). In such instance, appropriately longer integration time is necessary to detect the unstable solutions.

This issue is illustrated in Fig. 1. We choose one of the best fits with initial osculating, astrocentric Keplerian elements at the epoch of the first observation in terms of tuples $(m$ [mj], a [AU], e , ω [deg], \mathcal{M} [deg]): (0.593, 0.519, 0.0058, 303.360, 95.060), (0.558, 1.615, 0.101, 315.621, 70.279), and (0.690, 3.193, 0.26111, 255.848, 142.886) for planets b, c, and d, respectively. These initial conditions had $(\chi^2_\nu)^{1/2} \approx 0.98$ and an rms about 4 m/s. In the time range covered by the GAMP integrations (and up to $\sim 10^4 P_d$, i.e. $\sim 60,000$ yr), the configuration appears strictly regular because the indicator quickly converges to 2 (the top-left panel in Fig 1). Nevertheless, after the transient time, the MEGNO starts to grow linearly at the rate of $\sigma/2 \sim 2 \cdot 10^{-4} \text{ yr}^{-1}$ (where σ is the MLCE of the solution, see bottom-left panel in Fig. 1). Actually, after a relatively long time ~ 15 Myr, the chaotic motion leads to a collision between planets c and d (the top-right panel) due to a sudden increase of both eccentricities up to 0.6. The elimination of such solutions during an extensive GAMP-like search on a Myrs interval would be very difficult.

Looking for the source of such dramatically unstable behavior, we perform the frequency analysis of the orbits with the MFT by Sidlichovský & Nesvorný (1997). Denoting the proper mean motions by n_b, n_c , and n_d , respectively, we found that

$$n_b - 8n_c + 7n_d \approx -0.4^\circ/\text{yr},$$

clearly indicating the three-body MMR of the first order, and we label it with $+1b : -8c : +7d$. The time evolution of the critical argument $\theta = \lambda_b - 8\lambda_c + 7\lambda_d$ is illustrated in the bottom-right panel of Fig. 1. The circulation of the critical angle alternates with libration, indicating the separatrix crossings that explain chaotic evolution.

The presented example has inspired us to follow a two-stage procedure in modeling the RV data. First, with a GAMP-like code we look for many best-fit solutions, ideally, approximating the global shape of $(\chi^2_\nu)^{1/2}$ and simultaneously stable, at least over a relatively short period of time. At that stage the stability constraints cannot be tight, not only due to significant CPU requirements but also because we should not discard weakly chaotic solutions. Such configurations may be bounded over very long time, longer by orders of magnitude than their Lyapunov time $T_L = 1/\sigma$. In the next step, we either refine the search in a zone bounded by the previously found fits with much longer integration times (still numerically expensive), or we examine each fit with long-term direct integrations

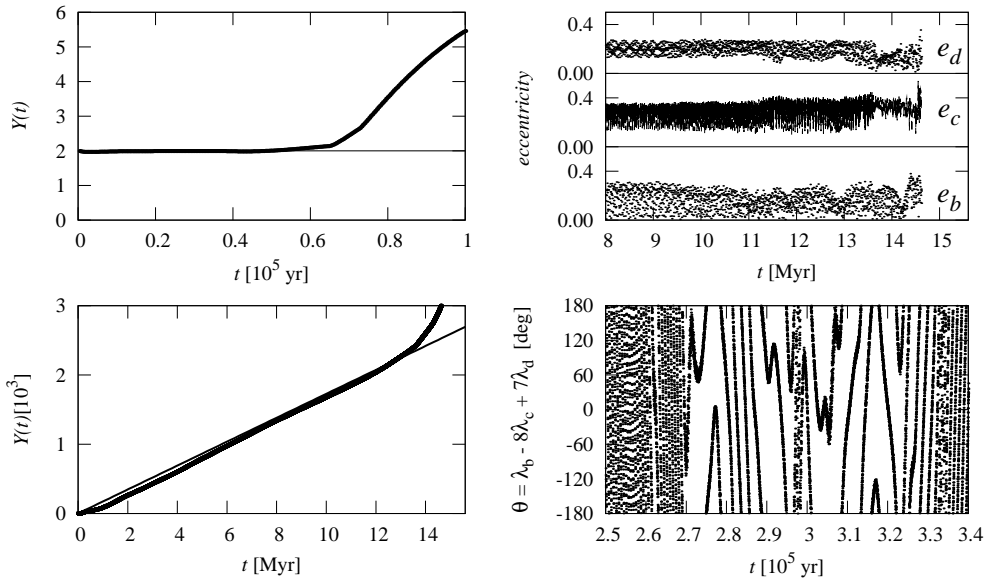


Figure 1. Evolution of the HD 37124 system selected best fit related to the three-body MMR (initial conditions listed in the text). Left: evolution of MEGNO over a short (top) and a long (bottom) time. The straight line is the least-square fit to $Y(t) = (\sigma/2)t + b$. Top right: contact eccentricities during ~ 15 Myr. Bottom right: the critical argument of the three-body MMR $+1b : -8c : +7d$.

and/or evaluate a fast indicator signature, like the MLCE, Spectral Number, or the diffusion of fundamental frequencies.

Here, for each solution with $(\chi^2_{\nu})^{1/2} < 1.1$, we computed its MEGNO signature. The integration time span is about of 37 Myr – long enough to detect the relevant chaotic three-body resonances and strong secular resonances. Here, and in the experiments described later on, we use the SBAB3 integrator scheme by Laskar & Robutel (2001). The time-step is 4 days. The secular periods in the given range of a_d are quite short, $\sim 10^4$ yr, nevertheless we can expect that dynamical effects of potentially active secular resonances could be detected after thousands of such characteristic periods, hence counted in 10^6 – 10^7 yr. Figure 2 illustrates the results. The quality of fits in terms of $(\chi^2_{\nu})^{1/2}$ is marked by the size of circles (better fits have larger circles). Red (medium grey) circles are for stable, quasi-periodic solutions. In that case the system may be stable over a very long time. Blue (dark grey) circles are for chaotic solutions that led to collisions between planets and that did not survive during the integration time (the integrations are interrupted if any of the eccentricities increases above 0.66). Finally, small yellow (light grey) circles mark all configurations (not necessarily regular) that survived, remaining bounded during the maximal integration time. Clearly, most of solutions with initial $e_d > 0.2$ are both chaotic and unbounded. Nevertheless, some chaotic solutions appear on the borders of stable regions as well. Generally, the distribution of fits gives us a clear image of the border of global instability of the system, relatively far from the collision zone.

3.2 Fine structure of the phase space

Figure 3 compares the sensitivity of MEGNO and the Spectral Number when we use the same integration time, $\sim 10^5$ yr $\approx 1.6 \cdot 10^4 P_d$. In the case of the SN map, we did the FFT on $N = 2^{19}$ steps of 64 d, counting the number of spectral lines above 1% of the largest amplitude in the signal of $f(t) = a_c(t) \exp(i\lambda_c t)$, where a_c and λ_c denote the *contact* semi-major axis and mean longitude of planet c.

Both dynamical maps present the same region of the phase space, in the neighborhood of the best fit. Note, that this particular solution has been refined with GAMP integration over time $5 \sim 10^4 P_d$ that is about of 2 orders of magnitude longer than in the set of selected solutions. The resolution of the maps is the same: 480×120 data points; the map coordinates are usual astrocentric osculating Keplerian elements. Most of best-fits from Fig. 2 lie in the region covered by Fig. 3.

Both maps reveal a number of unstable resonances. Yet the SN map involves some artifacts (*moire*-like patterns) related to a low value of the noise level parameter p . Within the same integration time, the MEGNO map reveals relatively more fine details than SN. In particular, the sophisticated border of the collision zone appears to be more sharp and shifted towards smaller e_d . We can also find some fine resonance lines entirely absent in the SN map. For instance, there is a fine structure on the right-hand side of the $8c : 3d$ MMR. In order to investigate that instability, we choose the initial condition marked with small crossed circle and labeled with **a**. The results of the MFT frequency analysis of this solution tell us that the structure is related to the $+2b : -12c : +3c$ MMR. The time evolution of the related critical argument is illustrated Fig. 8a.

Next, we computed close-ups of the dynamical map within the rectangle labeled I in Fig. 3. These maps are shown in Fig. 4. This time we increased p to 5% and the total number of steps has been doubled ($N = 2^{20}$) in order to avoid the moire artifacts. But once again the “concurrent” MEGNO map (the right panel of Fig. 4) calculated over the same total time seems to offer a better representation of the phase space. Interestingly, the best fit data (Table 1) seem to lie on the border of a chaotic zone spanned by many overlapping resonances. A close-up of that area, marked with rectangle II in Fig. 4, is shown in Fig. 5. Clearly, even a very small change of parameters of the outermost planet may push the system into a strongly chaotic state. It also illustrates the good performance of the GAMP algorithm that was able to locate and preserve the fit in an extremely narrow island of stable motions.

A closer inspection of the area III in Fig. 4 reveals a multi-

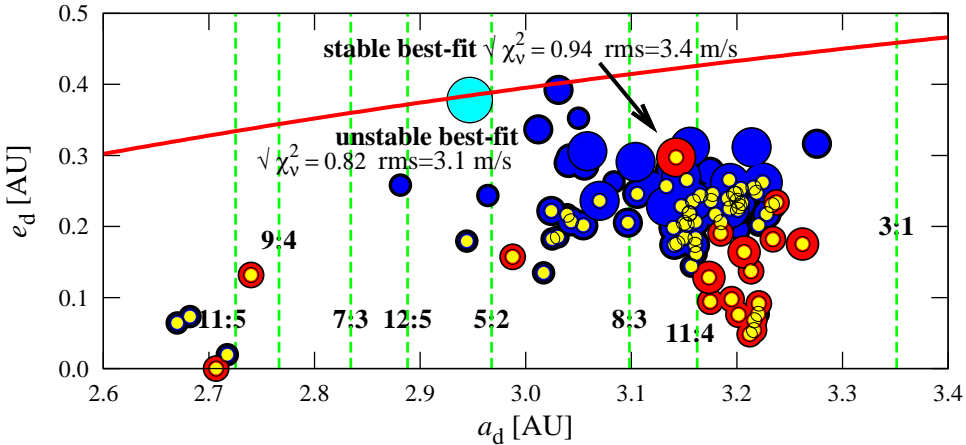


Figure 2. The long-term stability of the best-fits obtained in the GAMP search by Goździewski et al. (2006). The osculating elements at the epoch of the first observation (JD 2,450,420.047) are projected onto the (a_d, e_d) -plane (i.e., the semi-major axis vs the eccentricity of the outermost planet). The quality of fits in terms of $(\chi^2_v)^{1/2} < 1.1$ and $\text{rms} < 4 \text{ m/s}$ is marked by the size of blue (dark grey) and red (medium grey) circles (larger circles have better fit quality). The best fit, self-consistent Newtonian configuration obtained without stability constraints, in terms of quintuples (m [m_J], a [AU], e , ω [deg], \mathcal{M} [deg]) at the epoch of the first observation, is (0.619, 0.519, 0.088, 141.91, 257.34), (0.565, 1.663, 0.104, 331.88, 67.71), and (0.732, 2.947, 0.378, 283.33, 95.32) for planets b, c, and d, respectively, with velocity offset 7.53 m/s. The blue circles are for chaotic solutions that did not survive the integration time of ~ 37 Myr. The red circles are for regular solutions — in that case the MEGNO converged to 2. The small yellow (light grey) circles mark configurations that survived the integration. The best *stable* fit found is marked with an arrow, its osculating elements are given in Table 1. Some dominant MMRs of planets c and d are marked with dashed vertical lines, according to the third Kepler law, and labeled accordingly. The red curve marks the collision line of the two outermost orbits.

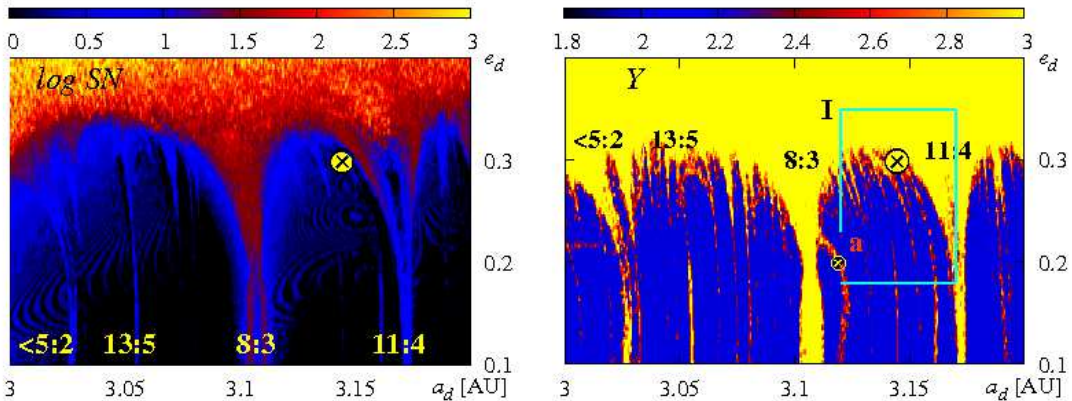


Figure 3. Dynamical maps of the Spectral Number (left) and the MEGNO indicator (right) computed in the neighborhood of the best-fit solution to the RV data of HD 37124 with the integration time $\sim 10^5$ yr. The elements of the best fit (see Table 1) are labeled with the crossed circle. The rectangle (I) marks the borders of the close-up shown in Fig. 4. The stability of orbits is color-coded: in both maps, yellow (pale grey) means strongly chaotic and unstable solutions; regular configurations are marked black in the SN-map and dark blue (dark grey) in the MEGNO map.

tude of weakly unstable solutions. To show such structures in more detail, we computed a close-up of that area (Fig. 6). The resolution of the maps is 200×200 data points, the integration interval is $\sim 3 \cdot 10^5$ yr $\approx 5 \cdot 10^4 P_d$. The time step at the left column is 16 days and it provides the relative error of the total energy at the level of 10^{-8} . Apparently, in spite of relatively short integration time, the map uncovers sophisticated structure of the two-body and three-body resonances. To identify some of them, we choose initial condition marked by small crossed circles and labeled in the map with **b**, **c**, and **d**, respectively.

For initial condition **b** we found that $n_b - 11n_c + 15n_d \approx -0.1^\circ/\text{yr}$, i.e., indicating three-body MMR $+1b : -11c : +15d$; for initial condition **c** we have got $10n_c - 27n_d \approx -0.3^\circ/\text{yr}$, corresponding to the $+10c : -27d$ MMR of the outer giants; and for initial condition **d** we have $n_b - n_c - 12n_d \approx -0.2^\circ/\text{yr}$, indicating the three-

body $+1b : -1c : -12d$ MMR, respectively. All these resonances excite chaotic configurations. That can be demonstrated through observing the time evolution of their critical angles (see Fig. 8b,c,d). In all those instances, we found that the libration alternates with circulation of these angles, hence confirming that the relevant configurations are close to the resonance separatrices.

A particularly interesting star-like structure can be seen around the initial condition **d** (the upper-left panel in Fig. 6). In that area, the two-body $10c : 27d$ MMR and many weak three-body resonances are active, for instance, $+1b : -11c : +15d \approx -1.35^\circ/\text{yr}$, $+1b : -1c : -12d \approx -0.2^\circ/\text{yr}$, $+2b : -12c : +3d \approx -1.5^\circ/\text{yr}$, $+3b : -13c : -9d \approx -1.7^\circ/\text{yr}$, and $+10c : -27d \approx 1.2^\circ/\text{yr}$.

One might be tempted to attribute this sophisticated structure to the so called Arnold web (Cincotta 2002). Indeed, a closer look at the branches of the web shows new fine details and extremely

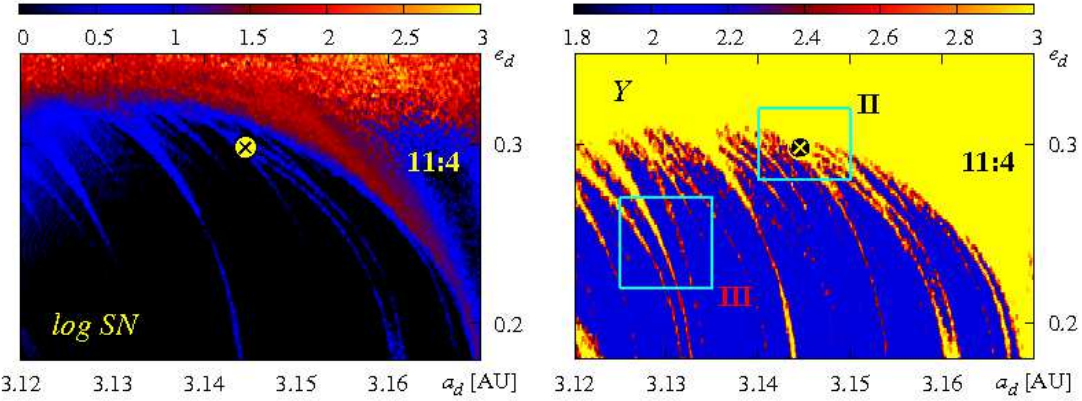


Figure 4. Dynamical maps in terms of the Spectral Number (the left panel) and the MEGNO indicator (the right panel) computed in the region marked with small rectangle I in Fig. 4. The integration time $\sim 3 \times 10^5$ yr is equivalent to $\sim 4.8 \cdot 10^4$ orbital periods of the outermost planet. The resolution of the maps 500×120 data points. The stability of orbits is color-coded, see the caption to the previous figure.

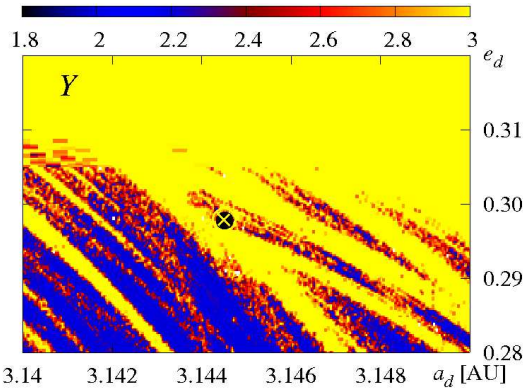


Figure 5. Dynamical maps in terms of the MEGNO indicator computed in the region marked by small rectangle in Fig. 4. The integration time is $\sim 3 \times 10^5$ yr that is equivalent to $\sim 4.8 \cdot 10^4$ orbital periods of the putative outermost planet. The resolution of the plot is 200×320 data points.

complex dynamical structure, in that zone, illustrated in the close-up map around initial condition **d**, Fig. 7. But the truth is that this particular structure is mostly spurious, and it occurred due to an improper choice of the integration step. To shed more light on that issue, we show the map of the relative error of the total energy (the left-bottom panel in Fig. 6). The coincidence of higher energy error streaks (bottom left) with instability patterns detected by MEGNO (top left) is not conclusive by itself, but when we recompute both maps using a smaller time step of 10 days (panels in the right column of Fig. 6), we notice that the web patterns of higher MEGNO disappear (Fig. 6, top right) and the energy error map significantly flattens (Fig. 6, bottom right). We conclude that two additional resonance lines that crossed at **d** were generated by the so-called ‘step-size resonances’ (Rauch & Holman 1999) between proper frequencies of the system and the sampling frequency of the constant step integrator. The effect of step-size resonance in a constant step integrator can be avoided either by using a sufficiently small integration step or by the application of high-order schemes. Unfortunately, both approaches lead to more time consuming algorithms.

As we could expect, the symplectic scheme outperforms the classical integration algorithms. For instance, we found the the MEGNO code driven by the Bulirsh-Gragg-Stoer ODEX integrator (Hairer & Wanner 1995) with the relative accuracy set to 10^{-13}

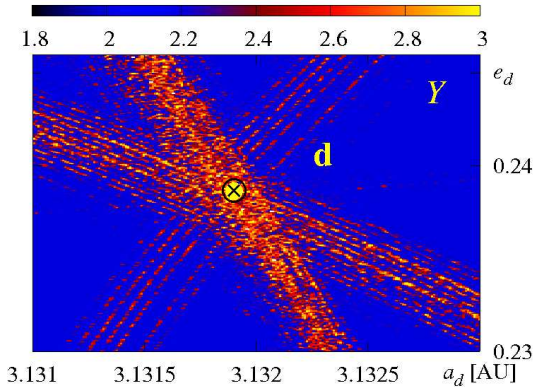


Figure 7. Close-up’s of the MEGNO dynamical map shown in the left panel of Fig. 6. The integration time $\sim 2 \times 10^5$ yr is equivalent to $\sim 3.2 \cdot 10^4$ orbital periods of the putative outermost planet d. The resolution is 200×480 points. The MEGNO is computed by the symplectic algorithm with the time-step of 16 days.

requires a similar CPU time, as the Laskar-Robutel SBAB3 scheme with 4 days step-size, but the former leads to a much larger, secularly growing energy error (which is larger by 2-3 orders of magnitude).

4 CONCLUSIONS

The use of Poincaré variables in the studies of the dynamics of close-to integrable planetary systems offers many advantages. The variables are canonical and offer a simple form of a reduced Hamiltonian. The Hamiltonian can be split into a sum of two separately integrable parts: the Keplerian term and a small perturbation. As such, it can serve to construct a symplectic integrator based on any modern composition method, including the recent ones invented by Laskar & Robutel (2001). The tangent map computed with the same integration scheme provides an efficient way of computing the estimate of maximal Lyapunov exponent in terms of relatively recent fast indicator MEGNO. The method proves to be much more efficient than general purpose integrators (like the Bulirsh-Stoer-Gragg method). Besides, it provides the conservation of the

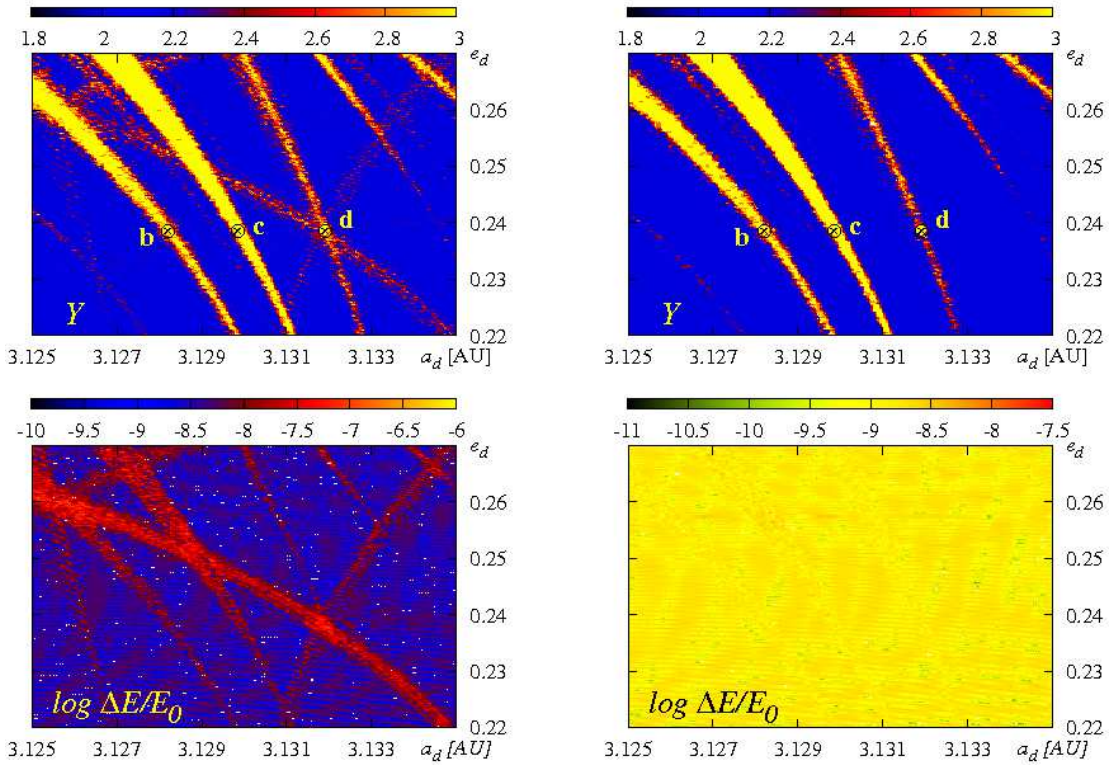


Figure 1:

Figure 6. Close-up's of the MEGNO dynamical map shown in Fig. 4 within rectangle labeled with III, illustrating the fine structure of the phase space. The integration time $\sim 3 \times 10^5$ yr is equivalent to $\sim 4.8 \cdot 10^4$ orbital periods of the putative outermost planet d. The resolution is 200×200 points. Panels in the top are for the MEGNO computed by the symplectic algorithm: the left panel is for the time-step of 16 days, the right panel if for the time step of 10 days. The bottom row is for the relative error of the total energy, for the same time steps, respectively.

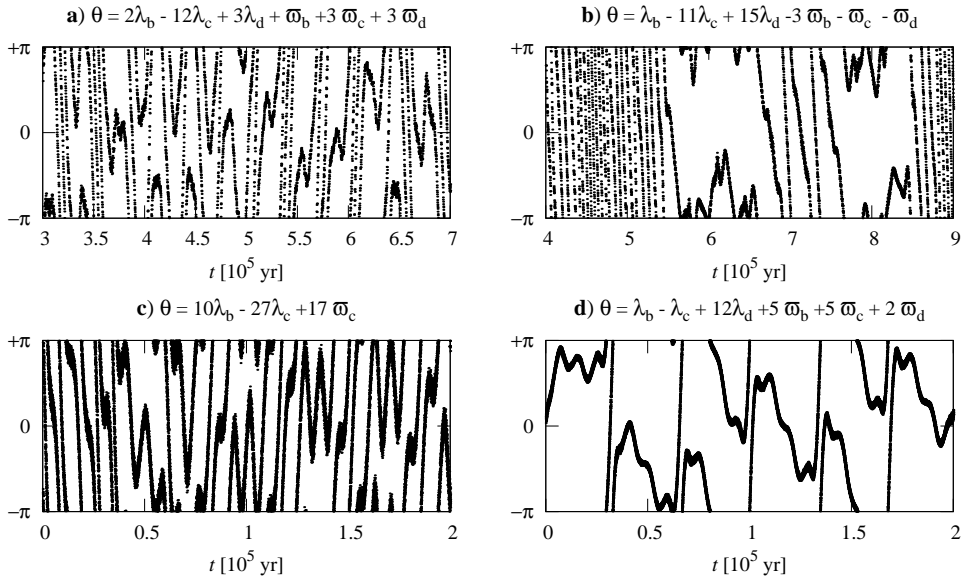


Figure 8. Time-evolution of the critical arguments of some resonances illustrated in the dynamical maps in Figs. 4 and 6. The panels are labeled accordingly with initial conditions marked by small crossed circles in these dynamical maps. See the text for more details.

grals of energy and the angular momentum that is crucial for solving the fine structure of the phase space. From the practical point of view, the symplectic algorithms are relatively simple for numerical implementation.

Using the numerical tools, we investigate the long term stability of extrasolar planetary system hosted by HD 37124. The orbital parameters in the set of our best, self-consistent Newtonian fits (Goździewski et al. 2006) are in accord with the discovery paper (Vogt et al. 2005). Nevertheless, the observational window of the system is still narrow and the derivation of the model consistent with observations is difficult and, in fact, uncertain. The dynamical maps reveal that the relevant region of the phase space, in the neighborhood of the mathematically best fit, is a strongly chaotic and unstable zone. The fitting algorithm (GAMP) that relies on eliminating strongly unstable fits finds solutions with a similar quality [in terms of $(\chi^2_v)^{1/2}$] that yields the formal solution. Moreover, they are shifted towards larger semi-major axes and much smaller eccentricities of the outermost planet. The orbital evolution of two outer planets is confined to a zone spanned by a number of low-order two-body and three-body MMRs. In particular, the three-body MMRs may induce very unstable behaviors that manifest themselves after many Myrs of an apparently stable and bounded evolution. To deal with such a problem, the stability of the best fits should be examined over a time-scale that is much longer than the one required when only the two-body MMRs are considered. In accord with the dynamical maps, the stable fits to the RV of HD 37124 should have small eccentricity of the outermost planet d, not larger than 0.2-0.3. Moreover, the stable configurations of the HD 37124 system are puzzling. The best-fit mathematical three-planet model is surprisingly distant, in the phase space of initial conditions, from the zone of stable solutions consistent with the RV. It remains possible that other bodies are present in the system and the three-planet model is not adequate to explain the RV variability, in spite that it provides apparently perfect fits. Yet, isolated initial conditions or even sets of best-fit solutions do not provide a complete answer on the system configuration. Then the fast indicator approach is essential and helpful to resolve the dynamical structure of the phase space.

The results of our experiments confirm and warn that all numerical methods should be applied with great care. All symplectic methods are constant step integrators. In that case one should be cautious about the possibility of generating spurious resonance webs. A proper way to avoid them is to repeat computations with a different integration step in order to detect step-dependent patterns.

5 ACKNOWLEDGMENTS

We thank David Nesvorný for a review and comments that improved that manuscript. This work is supported by KBN Grant No. 1P03D-021-29.

REFERENCES

Arnold V. I., 1978, Mathematical methods of classical mechanics. Graduate texts in mathematics, New York: Springer, 1978

Benettin G., Galgani L., Giorgilli A., Strelcyn J.-M., 1980, *Mecanica*, pp 9–30

Breiter S., Melendo B., Bartczak P., Wytrzyszczak I., 2005, *A&A*, 437, 753

Brumberg V., 1991, Essential Relativistic Celestial Mechanics. A. Hilger, Bristol-Philadelphia

Butler R. P., Tinney C. G., Marcy G. W., Jones H. R. A., Penny A. J., Apps K., 2001, *ApJ*, 555, 410

Chambers J. E., 1999, *MNRAS*, 304, 793

Cincotta P. M., 2002, *New Astronomy Review*, 46, 13

Cincotta P. M., Giordano C. M., Simó, C. 2003, *Physica D*, 182, 151

Cincotta P. M., Simó C., 2000, *A&A Suppl. Ser.*, 147, 205

Deprit A., 1983, *Celestial Mech. & Dyn. Astron.*, 30, 181

Duncan M. J., Levison H. F., Lee M. H., 1998, *AJ*, 116, 2067

Ferraz-Mello S., Michtchenko T. A., Beauge C., 2004, *ArXiv Astrophysics e-prints*

Froeschlé C., 1984, *Celestial Mech. & Dyn. Astron.*, 34, 95

Goździewski K., 2003, *A&A*, 398, 315

Goździewski K., Konacki M., 2004, *ApJ*, 610, 1093

Goździewski K., Konacki M., Maciejewski A. J., 2006, *ApJ*, 645, 688

Guzzo M., 2006, *Icarus*, 181, 475

Hagihara Y., 1970, Celestial Mechanics. MIT Press, Cambridge, pp 466–476

Hairer E., Wanner G., 1995, <http://www.unige.ch/math/folks/hairer/>

Hori G.-I., 1985, in *Resonances in the Motion of Planets, Satellites and Asteroids Mutual perturbations of 1:1 commensurable small bodies with the use of the canonical relative coordinates. part i*. IAG-USP, São Paulo, pp 53–66

Laskar J., 1990, in *Modern Methods in Celestial Mechanics Systèmes de variables et éléments*. Editions Frontières, Gif-sur-Yvette, pp 63–87

Laskar J., 1991, in *Predictability, Stability and Chaos in N-Body Dynamical Systems Systèmes de variables et éléments*. Plenum Press, New York, pp 93–114

Laskar J., 1993, *Celestial Mech. & Dyn. Astron.*, 56, 191

Laskar J., Robutel P., 2001, *Celestial Mech. & Dyn. Astron.*, 80, 39

Lissauer J. J., 1999, *Rev. Mod. Phys.*, 71, 835

Michtchenko T., Ferraz-Mello S., 2001, *ApJ*, 122, 474

Mikkola S., Innanen K., 1999, *Celestial Mech. & Dyn. Astron.*, 74, 59

Morbidelli A., 2002, *Modern celestial mechanics : aspects of solar system dynamics*. Taylor & Francis, London

Murray N., Holman M., Potter M., 1998, *AJ*, 116, 2583

Nesvorný D., Morbidelli A., 1998, *AJ*, 116, 3029

Nesvorný D., Morbidelli A., 1999, *Celestial Mech. & Dyn. Astron.*, 71, 243

Poincaré H., 1896, *C. R. Acad. Sci. Paris*, 123, 1031

Poincaré H., 1905, *Leçons de Mécanique Céleste*. Gauthier-Villars, Paris, p. 51

Rauch K. P., Holman M., 1999, *AJ*, 117, 1087

Šidlichovský M., Nesvorný D., 1997, *Celestial Mech. & Dyn. Astr.*, 65, 137

Suzuki M., 1991, *J. Math. Phys.*, 32, 400

Szebehely V., 1984, *Celestial Mech. & Dyn. Astron.*, 34, 49

Vogt S. S., Butler R. P., Marcy G. W., Fischer D. A., Henry G. W., Laughlin G., Wright J. T., Johnson J. A., 2005, *ApJ*, 632, 638

Whittaker E. T., 1952, *A Treatise on the Analytical Dynamics of Particles and Rigid Bodies*. University Press, Cambridge

Wisdom J., Holman M., 1991, *AJ*, 102, 1528

Yuasa M., Hori G., 1979, in *IAU Symp. 81: Dynamics of the Solar System New approach to the planetary theory*. pp 69–72